Acta Mechanica Sinica (2012) 28(6):1602–1616
DOI 10.1007/s10409-012-0153-0

RESEARCH PAPER

Validation and application of three-dimensional discontinuous deformation analysis with tetrahedron finite element meshed block

Jun Liu · Zheng Nan · Ping Yi

Received: 23 April 2012 / Revised: 16 July 2012 / Accepted: 27 July 2012

Abstract In the last decade, three dimensional discontinuous deformation analyses (3D DDA) has attracted more and more attention of researchers and geotechnical engineers worldwide. The original DDA formulation utilizes a linear displacement function to describe the block movement and deformation, which would cause block expansion under rigid body rotation and thus limit its capability to model block deformation. In this paper, 3D DDA is coupled with tetrahedron finite elements to tackle these two problems. Tetrahedron is the simplest in the 3D domain and makes it easy to implement automatic discretization, even for complex topology shape. Furthermore, element faces will remain planar and element edges will remain straight after deformation for tetrahedron finite elements and polyhedral contact detection schemes can be used directly. The matrices of equilibrium equations for this coupled method are given in detail and an effective contact searching algorithm is suggested. Validation is conducted by comparing the results of the proposed coupled method with that of physical model tests using one of the most common failure modes, i.e., wedge failure. Most of the failure modes predicted by the coupled method agree with the physical model results except for 4 cases out of the total 65 cases. Finally, a complex rockslide example demonstrates the robustness and versatility of the coupled method.

The project was supported by the Key Project of Chinese National Programs for Fundamental Research and Development (2010CB731502) and the National Natural Science Foundation of China (50978745).

J. Liu · Z. Nan
School of Hydraulic Engineering,
Dalian University of Technology, 116024 Dalian, China

P. Yi (✉)
School of Civil Engineering,
Dalian University of Technology, 116024 Dalian, China
e-mail: yiping@dlut.edu.cn

Keywords Three-dimensional discontinuous deformation analysis · Finite element method · Coupled method · Validation

1 Introduction

Discontinuous deformation analysis (DDA) proposed by Shi [1, 2] in the late 1980s is an alternative to the commonly used discontinuity based discrete element method (DEM). However, unlike force based DEM, DDA is based on the minimization of total potential energy of the block assembly and shares many common features with finite element method (FEM). DDA incorporates dynamics, kinematics, and elastic deformability of the block, and models actual displacements of individual blocks using a time-step marching scheme. A review of validation studies on the DDA approach is provided by MacLaughlin and Doolin [3].

The original DDA formulation utilizes a linear displacement function to describe the block movement and deformation, and the stress and strain within any given block are constant across the whole region of the block. These constant values can be viewed as the average values of the actual stress and strain within a block. If the size of a block is small enough, this approach is acceptable, but for a large block where the variation of stress and strain within the block may be significant, it is definitely a poor representation. This limitation can be overcome by:

(1) The use of relatively exact displacement function with high order terms;

(2) Internal discretization by constant stress/strain DDA block with the introduction of internal springs to ensure continuity within each block;

(3) Finite element internal discretization of a block.

For the first approach, the early researches utilized second-order displacement function [4], third-order displacement function [5] and any order polynomial displacement function [6]. But the integration of potential energy

becomes so complicated that it is almost impossible to include many high order terms, and furthermore, even high order displacement functions may still be inadequate for a large block. For the second approach, Ke [7] glued small blocks together to form a larger block using artificial joints. Cheng and Zhang [8] used an automatic internal discretization scheme which generated triangular sub-blocks within a block and Ning et al. [9] adopted an advanced discretisation method to simulate rock failure problems. For the third approach, Shyu [10] reformulated DDA based on four-node isoparametric finite elements and Chang [11] analyzed nonlinear dynamic DDA using a finite element meshed block system. Jing et al. [12] modeled fractured rocks by DDA with internal discretization of deformable blocks using triangle or quadrilateral elements and Grayeli and Mortazavi [13] modified DDA using the second-order six-node triangular finite elements.

There is another limitation in the original DDA formulation related to the linear displacement function, which arises from the free expansion of block due to rotation. The change of block size would then result in contact detection difficulties because wrong vertex co-ordinates are determined. It is said that the block expansion can be more than 50% if the time-step is relatively large [8]. If a small time-step is used to control the amount of rotation, it will be prohibitively time consuming. In the literatures, two approaches have been proposed to solve the problem of block expansion:

(1) The use of relatively exact displacement function with nonlinear terms [8];

(2) The use of linear displacement function and post-correction or post-adjustment [14].

Although the previous work is mostly based on two dimensional (2D) DDA, there is an obvious need for a three dimensional (3D) model because the highly directional nature of jointed rock mass behavior makes the application of 2D DDA to many practical problems inappropriate. Therefore in the last decade, 3D DDA has attracted more and more attention of researchers and geotechnical engineers worldwide. Shi [15] and Liu et al. [16] provided basic formulations of matrices for different potential terms. Yeung et al. [17] and Moosavi et al. [18] highlighted the application of 3D DDA. Because the block contact detection is a very difficult and computationally demanding task in 3D models, many researches have been devoted to searching and calculating geometrical contacts in the 3D discontinuity-based problems [19–24].

In these researches, a 3D linear displacement function is still used. Similar to 2D DDA, 3D linear displacement function may also cause block expansion under rigid body rotation and thus its capability of modeling block deformation is limited. To overcome these limitations, some approaches have been attempted. Beyabanaki et al. [25] used second- and third-order displacement function to describe nonlinear distributions of stresses and strains within a discrete block. Liu and Kong [26] added trilinear (8-node) finite elements into 3D DDA and Beyabanaki et al. [27] added both trilinear and serendipity (20-node) hexahedron finite elements into 3D DDA. Although the post-contact adjustment technique [28] has also been proposed to tackle the free expansion problem in 3D DDA, it is actually suitable only for 2D DDA. The reason is that there is only one rotation degree of freedom (DOF) in 2D DDA however in 3D DDA, three coupled rotation DOFs exist. The Eulerian angle method is the appropriate method to describe rigid rotation in three dimensional spaces. But then the displacement function becomes a highly nonlinear function, which will also cause computation difficulties.

In this paper, 3D DDA is coupled with the tetrahedron finite element to tackle the problem of block expansion and to enhance DDA block's deformation ability. The tetrahedron element and hexahedron element are the basic three dimensional elements in FEM [29]. Although the hexahedron element is more accurate and the strain is not constant throughout the element [30], the tetrahedron element has the advantages of simplicity and adaptability to complex topology shape. Tetrahedron is the simplest in the 3D domain and it is easy to implement automatic discretization using the tetrahedron element. Furthermore, block faces may not remain planar for hexahedron finite elements or high order displacement functions after deformation, which will cause contact detection difficulties using existing 3D contact detection schemes. For tetrahedron finite elements, however, element faces will remain planar and element edges will remain straight after deformation and 3D polyhedral contact detection schemes can be used directly. Therefore, tetrahedron finite elements are appropriate for being meshed into 3D DDA blocks and Grayeli and Hatami [31] once did related research. In this paper the matrices of equilibrium equations for this coupled method are given in detail and an effective contact searching algorithm is suggested. The program code has been developed using Visual C++ with easily used preprocessor and post-processor. For validation, one of the most common failure modes, i.e., wedge failure, is analyzed by the coupled method and its results are compared with that of physical model tests (Yeung et al. [17]). Most of the failure modes predicted by the coupled method agree with the physical model results except for 4 cases out of the total 65 cases. Finally, a complex rockslide example demonstrates the robustness and versatility of the coupled method.

2 Combination of 3D DDA with tetrahedron finite element meshes

DDA shares many common features with FEM for stress and deformation analysis of a deformable continuum body and it is easy and natural to merge finite element mesh into a block. In the process of mesh generation, the meshes of the elements and boundaries of the blocks need to be formed separately, and then both are merged together with the same

nodal number between the elements, but with different nodal numbers between the boundaries of the blocks. Within every block, the displacement is continuous and between blocks, rigid rotation, sliding, fracture opening and complete detachments could occur. Figure 1 shows a two-blocks system with tetrahedron elements mesh.

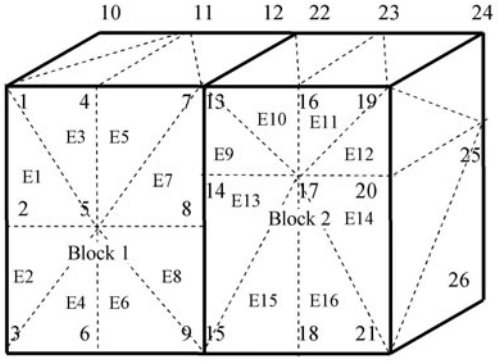

Fig. 1 Mesh of elements and blocks

By adding finite element mesh into each block, it is possible to take advantage of both the continuous properties of 3D FEM and the discontinuous characteristics of 3D DDA, thereby being able to address engineering problems more flexibly. The coupled method also uses time steps for both static and dynamic analyses. The large displacements of blocks and the large relative movements between blocks are accumulated over many time steps. At the end of each time step, the block system satisfies equilibrium conditions and contact conditions, i.e., the no-penetration and no-tension criteria and the Coulomb–Mohr failure criterion.

2.1 Simultaneous equation

DDA conforms to the principle of minimum total potential energy and the total potential energy is the summation of all potential energy sources for each block, including the strain energy of the induced and initial stresses, the external work of inertia force, point loading, body force, and the displacement constraint, as well as the potential interaction between two blocks such as normal and shear contacts. The nodal matrices of stiffness and force are then formed by taking the derivatives with respect to the displacement variables from the corresponding potential energy. Taking the direct summation of these individual submatrices to form the global stiffness matrix $\boldsymbol{K}$ and the global force vector $\boldsymbol{F}$, the simultaneous equations of equilibrium are then established in the following form

$$\begin{bmatrix} \boldsymbol{K}_{11} & \boldsymbol{K}_{12} & \cdots & \boldsymbol{K}_{1n} \\ \boldsymbol{K}_{21} & \boldsymbol{K}_{22} & \cdots & \boldsymbol{K}_{2n} \\ \vdots & \vdots & \ddots & \vdots \\ \boldsymbol{K}_{n1} & \boldsymbol{K}_{n2} & \cdots & \boldsymbol{K}_{nn} \end{bmatrix} \begin{Bmatrix} \boldsymbol{D}_1 \\ \boldsymbol{D}_2 \\ \vdots \\ \boldsymbol{D}_n \end{Bmatrix} = \begin{Bmatrix} \boldsymbol{F}_1 \\ \boldsymbol{F}_2 \\ \vdots \\ \boldsymbol{F}_n \end{Bmatrix}, \tag{1}$$

where n is the number of nodes, $\boldsymbol{D}_i$ is the unknown displacement vector of the i-th node and is a 3×1 submatrix for the three dimensional case. $\boldsymbol{K}_{ij}$ is a 3×3 stiffness submatrix and $\boldsymbol{F}_i$ is a 3×1 submatrix of resultant general forces acting on the i-th node.

2.2 Displacement approximation of a tetrahedron element

Figure 2 shows a 3D tetrahedron element with vertices i, j, k and m. Each vertex or node has three displacement components $\boldsymbol{d}_r = \{u_r, v_r, w_r\}^{\mathrm{T}}$ $(r = i, j, k, m)$. So for the element, $\boldsymbol{D}_{\mathrm{e}} = \{d_i, d_j, d_k, d_m\}^{\mathrm{T}}$ is a 12×1 vector. The displacement field $\{u\ v\ w\}^{\mathrm{T}}$ of the tetrahedron element can be described as

$$\begin{Bmatrix} u \\ v \\ w \end{Bmatrix} = \begin{bmatrix} N_i & 0 & 0 & N_j & 0 & 0 & N_k & 0 & 0 & N_m & 0 & 0 \\ 0 & N_i & 0 & 0 & N_j & 0 & 0 & N_k & 0 & 0 & N_m & 0 \\ 0 & 0 & N_i & 0 & 0 & N_j & 0 & 0 & N_k & 0 & 0 & N_m \end{bmatrix} \times \begin{Bmatrix} \boldsymbol{d}_i \\ \boldsymbol{d}_j \\ \boldsymbol{d}_k \\ \boldsymbol{d}_m \end{Bmatrix} = \boldsymbol{N}_{\mathrm{e}}\boldsymbol{D}_{\mathrm{e}}, \tag{2}$$

where N_r (x, y, z) $(r = i, j, k, m)$ is the shape function of a tetrahedron element [29] and $\boldsymbol{N}_{\mathrm{e}}$ is a 3×12 matrix.

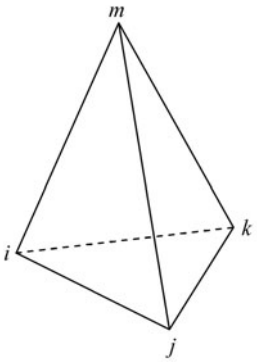

Fig. 2 Geometry of a tetrahedron element

2.3 Stiffness submatrix

From the displacement field, the strain field of a tetrahedron element is

$$\boldsymbol{\varepsilon}_{\mathrm{e}} = \begin{Bmatrix} \varepsilon_x \\ \varepsilon_y \\ \varepsilon_z \\ \gamma_{xy} \\ \gamma_{yz} \\ \gamma_{zx} \end{Bmatrix}$$

$$= \begin{Bmatrix} \dfrac{\partial u}{\partial x} \\ \dfrac{\partial v}{\partial y} \\ \dfrac{\partial w}{\partial z} \\ \dfrac{\partial u}{\partial y} + \dfrac{\partial v}{\partial x} \\ \dfrac{\partial v}{\partial z} + \dfrac{\partial w}{\partial y} \\ \dfrac{\partial w}{\partial x} + \dfrac{\partial u}{\partial z} \end{Bmatrix} = \boldsymbol{B}_{\mathrm{e}} \boldsymbol{D}_{\mathrm{e}}, \tag{3}$$

where $\boldsymbol{B}_{\mathrm{e}}$ is the geometrical matrix of the element and has the following form

$$\boldsymbol{B}_{\mathrm{e}} = [\boldsymbol{B}_i \ \ \boldsymbol{B}_j \ \ \boldsymbol{B}_k \ \ \boldsymbol{B}_m]_{6\times 12}, \tag{4}$$

where

$$\boldsymbol{B}_r = \begin{bmatrix} \dfrac{\partial N_r}{\partial x} & 0 & 0 \\ 0 & \dfrac{\partial N_r}{\partial y} & 0 \\ 0 & 0 & \dfrac{\partial N_r}{\partial z} \\ \dfrac{\partial N_r}{\partial y} & \dfrac{\partial N_r}{\partial x} & 0 \\ 0 & \dfrac{\partial N_r}{\partial z} & \dfrac{\partial N_r}{\partial y} \\ \dfrac{\partial N_r}{\partial z} & 0 & \dfrac{\partial N_r}{\partial x} \end{bmatrix}, \qquad r = i,\ j,\ k,\ m. \tag{5}$$

The stress–strain relationship is assumed to be linear at each time step and the stress field of the element is written as

$$\boldsymbol{\sigma}_{\mathrm{e}} = \begin{Bmatrix} \sigma_x \\ \sigma_y \\ \sigma_z \\ \tau_{xy} \\ \tau_{yz} \\ \tau_{zx} \end{Bmatrix} = \boldsymbol{E}_{\mathrm{e}} \boldsymbol{\varepsilon}_{\mathrm{e}}, \tag{6}$$

where $\boldsymbol{E}_{\mathrm{e}}$ is the elastic matrix of the element and has the following form for isotropic elastic material

$$\boldsymbol{E}_{\mathrm{e}} = \frac{E}{2(1+\mu)(1-2\mu)} \times \begin{bmatrix} 2(1-\mu) & 2\mu & 2\mu & 0 & 0 & 0 \\ 2\mu & 2(1-\mu) & 2\mu & 0 & 0 & 0 \\ 2\mu & 2\mu & 2(1-\mu) & 0 & 0 & 0 \\ 0 & 0 & 0 & 1-2\mu & 0 & 0 \\ 0 & 0 & 0 & 0 & 1-2\mu & 0 \\ 0 & 0 & 0 & 0 & 0 & 1-2\mu \end{bmatrix}, \tag{7}$$

where E and μ are Young's modulus and Poisson's ratio, respectively.

At each time step, the elastic strain energy stored by the stresses of the element is

$$\begin{aligned} \Pi_{\mathrm{e}} &= \frac{1}{2} \iiint_{v_{\mathrm{e}}} \boldsymbol{\varepsilon}_{\mathrm{e}}^{\mathrm{T}} \boldsymbol{\sigma}_{\mathrm{e}} \,\mathrm{d}x\,\mathrm{d}y\,\mathrm{d}z \\ &= \frac{1}{2} \boldsymbol{D}_{\mathrm{e}}^{\mathrm{T}} \iiint_{v_{\mathrm{e}}} \boldsymbol{B}_{\mathrm{e}}^{\mathrm{T}} \boldsymbol{E}_{\mathrm{e}} \boldsymbol{B}_{\mathrm{e}} \,\mathrm{d}x\,\mathrm{d}y\,\mathrm{d}z \cdot \boldsymbol{D}_{\mathrm{e}}. \end{aligned} \tag{8}$$

After taking derivatives with respect to displacement variables from the strain energy Π_{e}, the 12×12 element stiffness matrix $\boldsymbol{K}_{\mathrm{e}}$ with the following form is added to the global stiffness matrix in the simultaneous equations

$$\boldsymbol{K}_{\mathrm{e}} = \frac{\partial^2 \Pi_{\mathrm{e}}}{\partial \boldsymbol{D}_{\mathrm{e}}^2} = \iiint_{v_{\mathrm{e}}} \boldsymbol{B}_{\mathrm{e}}^{\mathrm{T}} \boldsymbol{E}_{\mathrm{e}} \boldsymbol{B}_{\mathrm{e}} \,\mathrm{d}x\,\mathrm{d}y\,\mathrm{d}z\,. \tag{9}$$

2.4 Initial stress submatrix

In DDA, the computed stresses at the previous time step will be transferred to the next step as the initial stress loading. For an initial stress field $\boldsymbol{\sigma}_{0_{\mathrm{e}}} = \{\sigma_x^0,\ \sigma_y^0,\ \sigma_z^0,\ \tau_{xy}^0,\ \tau_{yz}^0,\ \tau_{zx}^0\}_{\mathrm{e}}^{\mathrm{T}}$, the potential energy of the element is described as

$$\begin{aligned} \Pi_{\sigma} &= \iiint_{v_{\mathrm{e}}} \boldsymbol{\varepsilon}_{\mathrm{e}}^{\mathrm{T}} \boldsymbol{\sigma}_{0_{\mathrm{e}}} \,\mathrm{d}x\,\mathrm{d}y\,\mathrm{d}z \\ &= \boldsymbol{D}_{\mathrm{e}}^{\mathrm{T}} \iiint_{v_{\mathrm{e}}} \boldsymbol{B}_{\mathrm{e}}^{\mathrm{T}} \boldsymbol{\sigma}_{0_{\mathrm{e}}} \,\mathrm{d}x\,\mathrm{d}y\,\mathrm{d}z\,. \end{aligned} \tag{10}$$

By taking the derivatives from the potential energy Π_{σ}, the 12×1 element force matrix $\boldsymbol{F}_{\mathrm{e}}$ with the following form is added to the global force matrix in the simultaneous equations

$$\boldsymbol{F}_{\mathrm{e}} = -\frac{\partial \Pi_{\sigma}}{\partial \boldsymbol{D}_{\mathrm{e}}} = -\iiint_{v_{\mathrm{e}}} \boldsymbol{B}_{\mathrm{e}}^{\mathrm{T}} \boldsymbol{\sigma}_{0_{\mathrm{e}}} \,\mathrm{d}x\,\mathrm{d}y\,\mathrm{d}z\,. \tag{11}$$

2.5 Inertia force submatrix

Denote $\{u(x,y,z,t),\ v(x,y,z,t),\ w(x,y,z,t)\}^{\mathrm{T}}$ as the time-dependent displacements of any point (x, y, z) of the element. The inertia force per unit volume is

$$\begin{Bmatrix} f_x \\ f_y \\ f_z \end{Bmatrix} = -\rho \frac{\partial^2}{\partial t^2} \begin{Bmatrix} u(x,y,z,t) \\ v(x,y,z,t) \\ w(x,y,z,t) \end{Bmatrix}, \tag{12}$$

where ρ is the mass per unit volume. The potential energy of the inertia force of the element is

$$\Pi_{\mathrm{i}} = -\iiint_{v_{\mathrm{e}}} \{u\ v\ w\} \begin{Bmatrix} f_x \\ f_y \\ f_z \end{Bmatrix} \mathrm{d}x\,\mathrm{d}y\,\mathrm{d}z\,. \tag{13}$$

The acceleration is assumed to be constant at each time step. $\boldsymbol{D}(0)_{\mathrm{e}} = \boldsymbol{0}$ and $\boldsymbol{D}(\Delta)_{\mathrm{e}} = \boldsymbol{D}_{\mathrm{e}}$ are the displacements at the beginning and the end of the time step, respectively, and Δ is the time interval, then

$$\begin{aligned} \boldsymbol{D}_{\mathrm{e}} &= \boldsymbol{D}(\Delta)_{\mathrm{e}} \\ &= \boldsymbol{D}(0)_{\mathrm{e}} + \Delta\frac{\partial \boldsymbol{D}(0)_{\mathrm{e}}}{\partial t} + \frac{\Delta^2}{2}\frac{\partial^2 \boldsymbol{D}(0)_{\mathrm{e}}}{\partial t^2} \\ &= \Delta\frac{\partial \boldsymbol{D}(0)_{\mathrm{e}}}{\partial t} + \frac{\Delta^2}{2}\frac{\partial^2 \boldsymbol{D}(0)_{\mathrm{e}}}{\partial t^2}, \end{aligned} \tag{14}$$

$$\begin{aligned} \frac{\partial^2 \boldsymbol{D}(0)_{\mathrm{e}}}{\partial t^2} &= \frac{\partial^2 \boldsymbol{D}_{\mathrm{e}}}{\partial t^2} \\ &= \frac{2}{\Delta^2}\boldsymbol{D}_{\mathrm{e}} - \frac{2}{\Delta}\frac{\partial \boldsymbol{D}(0)_{\mathrm{e}}}{\partial t} \\ &= \frac{2}{\Delta^2}\boldsymbol{D}_{\mathrm{e}} - \frac{2}{\Delta}\boldsymbol{V}(0)_{\mathrm{e}}, \end{aligned} \tag{15}$$

in which

$$\boldsymbol{V}(0)_{\mathrm{e}} = \frac{\partial \boldsymbol{D}(0)_{\mathrm{e}}}{\partial t} \tag{16}$$

is the velocity at the beginning of the time step. Therefore, the potential energy of the inertia force of the element at the end of the time step can be rewritten as

$$\begin{aligned} \Pi_{\mathrm{i}} &= \rho \boldsymbol{D}_{\mathrm{e}}^{\mathrm{T}} \left(\iiint_{v_{\mathrm{e}}} \boldsymbol{N}_{\mathrm{e}}^{\mathrm{T}} \boldsymbol{N}_{\mathrm{e}}\,\mathrm{d}x\,\mathrm{d}y\,\mathrm{d}z \right) \frac{\partial^2 \boldsymbol{D}_{\mathrm{e}}}{\partial t^2} \\ &= \boldsymbol{D}_{\mathrm{e}}^{\mathrm{T}} \left(\iiint_{v_{\mathrm{e}}} \boldsymbol{N}_{\mathrm{e}}^{\mathrm{T}} \boldsymbol{N}_{\mathrm{e}}\,\mathrm{d}x\,\mathrm{d}y\,\mathrm{d}z \right) \left(\frac{2\rho}{\Delta^2}\boldsymbol{D}_{\mathrm{e}} - \frac{2\rho}{\Delta}\boldsymbol{V}(0)_{\mathrm{e}} \right). \end{aligned} \tag{17}$$

Because of the principle of minimum potential energy, the first-order derivatives of the potential energy is calculated as

$$\frac{\partial \Pi_{\mathrm{i}}}{\partial \boldsymbol{D}_{\mathrm{e}}} = \left(\iiint_{v_{\mathrm{e}}} \boldsymbol{N}_{\mathrm{e}}^{\mathrm{T}} \boldsymbol{N}_{\mathrm{e}}\,\mathrm{d}x\,\mathrm{d}y\,\mathrm{d}z \right) \left(\frac{2\rho}{\Delta^2}\boldsymbol{D}_{\mathrm{e}} - \frac{2\rho}{\Delta}\boldsymbol{V}(0)_{\mathrm{e}} \right). \tag{18}$$

In Eq. (18), there is an unknown variable vector $\boldsymbol{D}_{\mathrm{e}}$ and the expression can be transformed into two parts. The first part

$$\frac{2\rho}{\Delta^2} \left(\iiint_{v_{\mathrm{e}}} \boldsymbol{N}_{\mathrm{e}}^{\mathrm{T}} \boldsymbol{N}_{\mathrm{e}}\,\mathrm{d}x\,\mathrm{d}y\,\mathrm{d}z \right) = \boldsymbol{K}_{\mathrm{e}} \tag{19}$$

is added to the global stiffness matrix in the simultaneous equations. The second part

$$\frac{2\rho}{\Delta} \left(\iiint_{v_{\mathrm{e}}} \boldsymbol{N}_{\mathrm{e}}^{\mathrm{T}} \boldsymbol{N}_{\mathrm{e}}\,\mathrm{d}x\,\mathrm{d}y\,\mathrm{d}z \right) \boldsymbol{V}(0)_{\mathrm{e}} = \boldsymbol{F}_{\mathrm{e}} \tag{20}$$

is added to the global force matrix in the simultaneous equations. The initial velocity of the next time step is the velocity at the end of this time step and can be calculated as

$$\boldsymbol{V}(\Delta)_{\mathrm{e}} = \frac{2}{\Delta}\boldsymbol{D}_{\mathrm{e}} - \boldsymbol{V}(0)_{\mathrm{e}}. \tag{21}$$

2.6 Displacement constraint submatrix

Assuming the point (x, y, z) of the element is constrained with the displacement vector of $(u_{\mathrm{c}}, v_{\mathrm{c}}, w_{\mathrm{c}})$, one may use three very stiff springs with stiffness k along the x, y and z directions to compel the calculated displacement (u, v, w) to be $(u_{\mathrm{c}}, v_{\mathrm{c}}, w_{\mathrm{c}})$. The corresponding displacement vector of the spring is $(u_{\mathrm{c}} - u, v_{\mathrm{c}} - v, w_{\mathrm{c}} - w)$. Therefore, the potential energy related to the constrained spring is

$$\begin{aligned} \Pi_{\mathrm{c}} &= \frac{k}{2}\{u_{\mathrm{c}} - u \quad v_{\mathrm{c}} - v \quad w_{\mathrm{c}} - w\} \begin{Bmatrix} u_{\mathrm{c}} - u \\ v_{\mathrm{c}} - v \\ w_{\mathrm{c}} - w \end{Bmatrix} \\ &= \frac{k}{2}\{u_{\mathrm{c}} \ \ v_{\mathrm{c}} \ \ w_{\mathrm{c}}\} \begin{Bmatrix} u_{\mathrm{c}} \\ v_{\mathrm{c}} \\ w_{\mathrm{c}} \end{Bmatrix} - k\{u \ \ v \ \ w\} \begin{Bmatrix} u_{\mathrm{c}} \\ v_{\mathrm{c}} \\ w_{\mathrm{c}} \end{Bmatrix} \\ &\quad + \frac{k}{2}\{u \ \ v \ \ w\} \begin{Bmatrix} u \\ v \\ w \end{Bmatrix}. \end{aligned} \tag{22}$$

Substituting Eq. (2) into Eq. (22), we have

$$\begin{aligned} \Pi_{\mathrm{c}} &= \frac{k}{2}\{u_{\mathrm{c}} \ \ v_{\mathrm{c}} \ \ w_{\mathrm{c}}\} \begin{Bmatrix} u_{\mathrm{c}} \\ v_{\mathrm{c}} \\ w_{\mathrm{c}} \end{Bmatrix} - k\boldsymbol{D}_{\mathrm{e}}^{\mathrm{T}}\boldsymbol{N}_{\mathrm{e}}^{\mathrm{T}} \begin{Bmatrix} u_{\mathrm{c}} \\ v_{\mathrm{c}} \\ w_{\mathrm{c}} \end{Bmatrix} \\ &\quad + \frac{k}{2}\boldsymbol{D}_{\mathrm{e}}^{\mathrm{T}}\boldsymbol{N}_{\mathrm{e}}^{\mathrm{T}}\boldsymbol{N}_{\mathrm{e}}\boldsymbol{D}_{\mathrm{e}}. \end{aligned} \tag{23}$$

The 12×12 element stiffness matrix $\boldsymbol{K}_{\mathrm{e}}$ and the 12×1 element force matrix $\boldsymbol{F}_{\mathrm{e}}$ are obtained after taking the derivatives of displacement variables from the potential energy Π_{c} as follows

$$\boldsymbol{K}_{\mathrm{e}} = \frac{\partial^2 \Pi_{\mathrm{c}}}{\partial \boldsymbol{D}_{\mathrm{e}}^2} = k\boldsymbol{N}_{\mathrm{e}}^{\mathrm{T}}\boldsymbol{N}_{\mathrm{e}}, \tag{24a}$$

$$\boldsymbol{F}_{\mathrm{e}} = -\frac{\partial \Pi_{\mathrm{c}}}{\partial \boldsymbol{D}_{\mathrm{e}}} = k\boldsymbol{N}_{\mathrm{e}}^{\mathrm{T}} \begin{Bmatrix} u_{\mathrm{c}} \\ v_{\mathrm{c}} \\ w_{\mathrm{c}} \end{Bmatrix}. \tag{24b}$$

These matrices are then added to the simultaneous equilibrium equations.

2.7 Point loading submatrix

For DDA, a point loading force (F_x, F_y, F_z) can act on any point (x, y, z) of the element. The potential energy of the point loading is

$$\begin{aligned} \Pi_{\mathrm{p}} &= -(F_x u + F_y v + F_z w) \\ &= -\{u \ \ v \ \ w\} \begin{Bmatrix} F_x \\ F_y \\ F_z \end{Bmatrix} = -\boldsymbol{D}_{\mathrm{e}}^{\mathrm{T}}\boldsymbol{N}_{\mathrm{e}}^{\mathrm{T}} \begin{Bmatrix} F_x \\ F_y \\ F_z \end{Bmatrix}. \end{aligned} \tag{25}$$

By taking the derivatives from the potential energy Π_{p}, the 12×1 element force matrix $\boldsymbol{F}_{\mathrm{e}}$ with the following form is added to the global force matrix in the simultaneous equations

$$\boldsymbol{F}_{\mathrm{e}} = -\frac{\partial \Pi_{\mathrm{p}}}{\partial \boldsymbol{D}_{\mathrm{e}}} = \boldsymbol{N}_{\mathrm{e}}^{\mathrm{T}} \begin{Bmatrix} F_x \\ F_y \\ F_z \end{Bmatrix}. \tag{26}$$

2.8 Body force submatrix

When a constant body force (f_x, f_y, f_z) acts on the material volume of the element, the corresponding potential energy is

$$\begin{aligned} \Pi_{\mathrm{v}} &= -\iiint_{v_{\mathrm{e}}} \{u \;\; v \;\; w\} \begin{Bmatrix} f_x \\ f_y \\ f_z \end{Bmatrix} \mathrm{d}x\,\mathrm{d}y\,\mathrm{d}z \\ &= -\boldsymbol{D}_{\mathrm{e}}^{\mathrm{T}} \iiint_{v_{\mathrm{e}}} \boldsymbol{N}_{\mathrm{e}}^{\mathrm{T}}\,\mathrm{d}x\,\mathrm{d}y\,\mathrm{d}z \begin{Bmatrix} f_x \\ f_y \\ f_z \end{Bmatrix}. \end{aligned} \tag{27}$$

By taking the derivatives from the potential energy Π_v, the 12×1 element force matrix $\boldsymbol{F}_{\mathrm{e}}$ with the following form is added to the global force matrix in the simultaneous equations,

$$\boldsymbol{F}_{\mathrm{e}} = -\frac{\partial \Pi_{\mathrm{v}}}{\partial \boldsymbol{D}_{\mathrm{e}}} = \iiint_{v_{\mathrm{e}}} \boldsymbol{N}_{\mathrm{e}}^{\mathrm{T}}\,\mathrm{d}x\,\mathrm{d}y\,\mathrm{d}z \begin{Bmatrix} f_x \\ f_y \\ f_z \end{Bmatrix}. \tag{28}$$

3 Contact analysis and contact submatrix

In the previous section, the displacement and deformation of a single block or element and its contribution to the simultaneous equations are discussed. However, the blocks are not isolated. They are related with neighbouring blocks through contacting and separating and their movement must obey the contact criterion, i.e., "no penetration, no tension". The effect of the contact can be represented by applying two stiff contact springs in the normal and shear directions. The contact spring will be added if the blocks are in contact with each other and be deleted if the blocks are separated or the normal contact force is tensile. Open-close iteration is applied to identify the contact and arrange the correct locations of contact springs for each time step. It should be pointed out that Zheng and Jiang [32, 33] reformulate the 2D DDA as a mixed complementary problem (MiCP) or a variational inequality problem and then choose the path Newton method (PNM) to solve the problem and avoid the penalty factors and the open-close iteration.

After the contact points and the associated contact forces are determined, the normal contact and shear contact submatrices or friction force submatrices are then calculated and added to the global simultaneous equations. Therefore contact analysis is a critically important process in DDA and other discontinuity based numerical methods, and is just the prominent difference from continuum-based numerical methods. Meanwhile contact analysis is also a very difficult and computationally demanding calculation. A contact may appear between any two neighboring blocks, and may exist in any combination of vertices, edges and faces. Discrete elements, or blocks, may undergo large motions, causing opening and closing of joints, as well as sliding along the joint surfaces. Consequently, contacts among blocks need to be identified and continuously updated during the entire computation process. It is said that contact detection subroutines for 3D polyhedrons can easily take up to 80% of the total analysis time [20].

Contact analysis involves contact detection and contact interaction. The former is to find out the potential contacts and their possible types and positions so that proper physical laws can be applied to determine the contact forces in the latter. Contact detection begins with identifying neighboring blocks. Afterwards further examination would be implemented to determine if the blocks are indeed interfering or contacting. In the original 2D DDA, the direct testing approach is used and a completed block system kinematics is established [32]. For simply shaped 3D particles, such as spheres and ellipsoids, the contact detection is also easy. But for 3D polyhedrons, the contact detection can be quite cumbersome, to which many researches have been devoted [35–38].

3.1 Contact detection scheme

A preliminary effort to detect contact between discrete particles was made by Cundall [19], who proposed the common plane (CP) algorithm to detect and represent contacts in 2D polygonal and 3D polyhedral blocks system. A CP is a supposititious rigid plane that is hanged between two neighboring blocks by a string. When the two blocks are approaching to each other, the CP will rotate and translate and finally locate between the two blocks at an appropriate position (Fig. 3). If the two blocks are in contact, both will intersect the CP, and if they are not in contact, neither intersects the CP. By means of CP, the expensive particle-to-particle contact detection problem is reduced to a much faster plane-to-particle contact detection problem. Once the CP is established between two blocks, the normal to the CP defines the direction of the contact normal, which in turn defines the direction of the normal contact force between the two blocks. The sliding direction then lies in the CP.

Cundall [19] suggested an iterative procedure to find the CP:

(1) Get an initial guess of the CP. It is either the CP from the previous time step or the perpendicular bisector of the segment that connects the centroids of the two blocks;
(2) Calculate d_i, d_j and d_{ij}. d_i and d_j are respectively the distances of block i and block j to the CP and $d_{ij} = d_j - d_i$. If d_{ij} is greater than a small positive user-defined "tol-

erance", which can be set as twice the magnitude of the maximum displacement in each time step, the blocks are recognized as too far from each other to make a contact. Then the iterative process halts and no CP is developed. Otherwise, move the reference point to the midpoint of the segment connecting two closest vertices of the two blocks and two arbitrary orthogonal axes are chosen in the CP with their origin at the new reference point;

(3) The CP is then perturbed around each of the orthogonal axes in both negative and positive sense. If any perturbation produces a larger gap than that of the current CP, replace the new CP with the current one and go to iteration step (2). If all the perturbations produce smaller gap, rotate the current orthogonal axes for 45° and restart the perturbation. If still no larger gap is produced, start with a smaller perturbation until the CP is found with reasonable accuracy.

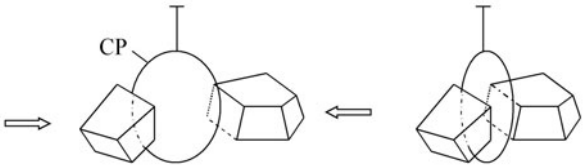

Fig. 3 Blocks and the common plane (CP)

The total number of iterations depends on the accuracy of the initial guess of the CP. In general, this algorithm requires a large number of iteration steps, and sometimes the iteration may fall into a saddle-point and a wrong CP is obtained.

Then Nezami et al. [20] proposed a fast common plane (FCP) identification algorithm for separate blocks and provided the proof. FCP approach recognizes that a CP has identifying characteristics, and in three-dimensions the candidate planes fall within four types, depending on the geometry of the separate blocks and their relative positions, which dramatically reduces the search space for the CP. For blocks in contact, Nezami et al. [20] suggested that an additional step has to be performed to temporarily separate the contact blocks by translating the two blocks in a direction perpendicular to the CP from the previous time step. The CP is then determined for this separated configuration.

Actually the FCP algorithm can be extended to all contact types and the four types of CP candidates are also valid for in-contact blocks or just-in-contact blocks. The proofs are given by Geng [39]. FCP algorithm is also an iterative algorithm, but the number of iterations here is usually very small and in most cases is less than 2. This is mainly because its iteration is done to locate the two closest vertices, rather than to determine the CP itself with "blind" perturbation in the conventional CP algorithm. In addition, the advanced FCP algorithm can be directly used to search contact pairs for both convex blocks and non-convex blocks in the coupled method because only the surface triangle facets on each block are the objects of contact identification. But in original 3D DDA or DEM, the non-convex blocks must be divided into several convex sub-blocks before using CP algorithm to identify contacts.

3.2 Contact submatrices

As shown in Fig. 4, element i and element j are two neighboring elements. P_1 (x_1, y_1, z_1) of element i and P_2 (x_2, y_2, z_2) of element j are the contact points and constitute a contact pair. (u_1, v_1, w_1) and (u_2, v_2, w_2) are the displacement increments of points P_1 and P_2, respectively. After the displacement increments, the two points move to P_1' and P_2'. The normal distance d_n from P_2' to P_1' along the normal vector of the CP, $\boldsymbol{n}(e_x, e_y, e_z)$, is

$$
\begin{aligned}
d_\mathrm{n} &= \boldsymbol{n} \cdot \overrightarrow{P_2' P_1'} \\
&= (\, e_x \;\; e_y \;\; e_z \,) \begin{Bmatrix} (x_1 + u_1) - (x_2 + u_2) \\ (y_1 + v_1) - (y_2 + v_2) \\ (z_1 + w_1) - (z_2 + w_2) \end{Bmatrix} \\
&= (\, e_x \;\; e_y \;\; e_z \,) \begin{Bmatrix} x_1 - x_2 \\ y_1 - y_2 \\ z_1 - z_2 \end{Bmatrix} + (\, e_x \;\; e_y \;\; e_z \,) \begin{Bmatrix} u_1 \\ v_1 \\ w_1 \end{Bmatrix} \\
&\quad -(\, e_x \;\; e_y \;\; e_z \,) \begin{Bmatrix} u_2 \\ v_2 \\ w_2 \end{Bmatrix} \\
&= s + (\, e_x \;\; e_y \;\; e_z \,) \boldsymbol{N}_i(x_1, y_1, z_1) \boldsymbol{D}_i \\
&\quad -(\, e_x \;\; e_y \;\; e_z \,) \boldsymbol{N}_j(x_2, y_2, z_2) \boldsymbol{D}_j \\
&= s + \boldsymbol{H}_i \boldsymbol{D}_i - \boldsymbol{G}_j \boldsymbol{D}_j .
\end{aligned} \tag{29}
$$

If $d_\mathrm{n} > 0$, it means penetration happens and a normal stiff spring should be added to compel $d_\mathrm{n} = 0$. Assume the spring stiffness is k_n, the potential energy of the normal spring is given by

$$
\begin{aligned}
\Pi_\mathrm{n} &= \frac{1}{2} k_\mathrm{n} d_\mathrm{n}^2 \\
&= \frac{1}{2} k_\mathrm{n} (s^2 + \boldsymbol{D}_i^\mathrm{T} \boldsymbol{H}_i^\mathrm{T} \boldsymbol{H}_i \boldsymbol{D}_i + \boldsymbol{D}_j^\mathrm{T} \boldsymbol{G}_j^\mathrm{T} \boldsymbol{G}_j \boldsymbol{D}_j \\
&\quad + 2 s \boldsymbol{H}_i \boldsymbol{D}_i - 2 s \boldsymbol{G}_j \boldsymbol{D}_j - 2 \boldsymbol{D}_i^\mathrm{T} \boldsymbol{H}_i^\mathrm{T} \boldsymbol{G}_j \boldsymbol{D}_j).
\end{aligned} \tag{30}
$$

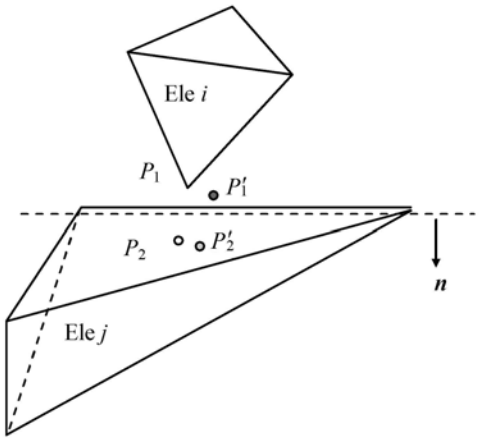

Fig. 4 Contact in 3D cases

The element matrices can be obtained by taking the derivatives from the potential energy Π_{n} with respect to the displacement variables

$$\begin{aligned}
&k_{\mathrm{n}}\boldsymbol{H}_i^{\mathrm{T}}\boldsymbol{H}_i \rightarrow \boldsymbol{K}_{ii},\\
&k_{\mathrm{n}}\boldsymbol{G}_j^{\mathrm{T}}\boldsymbol{G}_j \rightarrow \boldsymbol{K}_{jj},\\
&-k_{\mathrm{n}}\boldsymbol{H}_i^{\mathrm{T}}\boldsymbol{G}_j \rightarrow \boldsymbol{K}_{ij},\\
&-k_{\mathrm{n}}\boldsymbol{G}_j^{\mathrm{T}}\boldsymbol{H}_i \rightarrow \boldsymbol{K}_{ji},\\
&-k_{\mathrm{n}}s\boldsymbol{H}_i^{\mathrm{T}} \rightarrow \boldsymbol{F}_i,\\
&k_{\mathrm{n}}s\boldsymbol{G}_j^{\mathrm{T}} \rightarrow \boldsymbol{F}_j,
\end{aligned} \tag{31}$$

where $\boldsymbol{K}_{ii}$, $\boldsymbol{K}_{jj}$, $\boldsymbol{K}_{ij}$ and $\boldsymbol{K}_{ji}$ form four 12×12 element stiffness matrices, and are added to the global stiffness matrix in the simultaneous equilibrium equations. $\boldsymbol{F}_i$ and $\boldsymbol{F}_j$ form two 12×1 element force vectors, and are added to the global force vector in the simultaneous equilibrium equations.

The shear displacement d_{t} from P_2' to P_1' along the CP is calculated as

$$d_{\mathrm{t}} = \sqrt{\left|\overrightarrow{P_2'P_1'}\right|^2 - d_{\mathrm{n}}^2}. \tag{32}$$

If the following inequality is satisfied, which means no sliding is allowed, a shear contact spring is activated to enforce the lock of the contact pair.

$$F_{\mathrm{t}} < F_{\mathrm{n}}\tan\phi, \tag{33}$$

where F_{t} is the shear component of the contact force; ϕ is the friction angle of the discontinuity; and F_{n} is the normal contact force. Assume k_{t} is the shear spring stiffness, the potential energy of the shear spring is given by

$$\begin{aligned}
\Pi_{\mathrm{t}} &= \frac{1}{2}k_{\mathrm{t}}d_{\mathrm{t}}^2\\
&= \frac{1}{2}k_{\mathrm{t}}[(x_1 - x_2 + u_1 - u_2)^2 + (y_1 - y_2 + v_1 - v_2)^2\\
&\quad +(z_1 - z_2 + w_1 - w_2)^2 - d_{\mathrm{n}}^2].
\end{aligned} \tag{34}$$

By expanding and minimizing the potential energy Π_{t}, the following matrices can be added to the global stiffness matrix or the global force vector,

$$\begin{aligned}
&k_{\mathrm{t}}\boldsymbol{N}_i^{\mathrm{T}}\boldsymbol{N}_i \ - k_{\mathrm{t}}\boldsymbol{H}_i^{\mathrm{T}}\boldsymbol{H}_i \rightarrow \boldsymbol{K}_{ii},\\
&k_{\mathrm{t}}\boldsymbol{N}_j^{\mathrm{T}}\boldsymbol{N}_j - k_{\mathrm{t}}\boldsymbol{G}_j^{\mathrm{T}}\boldsymbol{G}_j \rightarrow \boldsymbol{K}_{jj},\\
&-k_{\mathrm{t}}\boldsymbol{N}_i^{\mathrm{T}}\boldsymbol{N}_j + k_{\mathrm{t}}\boldsymbol{H}_i^{\mathrm{T}}\boldsymbol{G}_j \rightarrow \boldsymbol{K}_{ij},\\
&-k_{\mathrm{t}}\boldsymbol{N}_j^{\mathrm{T}}\boldsymbol{N}_i + k_{\mathrm{t}}\boldsymbol{G}_j^{\mathrm{T}}\boldsymbol{H}_i \rightarrow \boldsymbol{K}_{ji},\\
&-k_{\mathrm{t}}\boldsymbol{N}_i^{\mathrm{T}}\begin{Bmatrix} x_1 - x_2\\ y_1 - y_2\\ z_1 - z_2 \end{Bmatrix} + k_{\mathrm{t}}s\boldsymbol{H}_i^{\mathrm{T}} \rightarrow \boldsymbol{F}_i,\\
&k_{\mathrm{t}}\boldsymbol{N}_j^{\mathrm{T}}\begin{Bmatrix} x_1 - x_2\\ y_1 - y_2\\ z_1 - z_2 \end{Bmatrix} - k_{\mathrm{t}}s\boldsymbol{G}_j^{\mathrm{T}} \rightarrow \boldsymbol{F}_j.
\end{aligned} \tag{35}$$

When the inequality (33) is not satisfied, which means the state of the contact is sliding, the shear spring is removed and a pair of equal and opposite frictional forces parallel to the sliding direction is applied on the contact face at the points. The frictional force is calculated from the normal contact compressive force from the previous iteration

$$F_{\mathrm{t}} = F_{\mathrm{n}}\tan\phi = k_{\mathrm{n}}|d_{\mathrm{n}}|\tan\phi. \tag{36}$$

The friction force will be applied along the projective direction of the previous displacement on the CP, $\boldsymbol{t}(t_x, t_y, t_z)$. At the end of the time step, the potential energy of the friction force is given by

$$\begin{aligned}
\Pi_{\mathrm{f}} &= F_{\mathrm{t}}[(x_1 - x_2 + u_1 - u_2)t_x + (y_1 - y_2 + v_1 - v_2)t_y\\
&\quad +(z_1 - z_2 + w_1 - w_2)t_z]\\
&= F_{\mathrm{t}}[(x_1 - x_2)t_x + (y_1 - y_2)t_y + (z_1 - z_2)t_z\\
&\quad +(\,t_x\ t_y\ t_z\,)\boldsymbol{N}_i\boldsymbol{D}_i - (\,t_x\ t_y\ t_z\,)\boldsymbol{N}_i\boldsymbol{D}_j].
\end{aligned} \tag{37}$$

By taking the derivatives from the potential energy Π_{f}, the 12×1 element friction force matrices with the following form are added to the global force vector in the simultaneous equations

$$\begin{aligned}
&-F_{\mathrm{t}}\boldsymbol{N}_i^{\mathrm{T}}(\,t_x\ t_y\ t_z\,)^{\mathrm{T}} \rightarrow F_i,\\
&F_{\mathrm{t}}\boldsymbol{N}_j^{\mathrm{T}}(\,t_x\ t_y\ t_z\,)^{\mathrm{T}} \rightarrow F_j.
\end{aligned} \tag{40}$$

4 Validation

In computational mechanics, any method must be thoroughly tested against real behaviour to establish its validity. To validate a method, one must demonstrate that the solution of a real problem by the method agrees well with an independent solution to the problem. The independent solution can be taken from physical model tests, field case histories or other validated numerical computational algorithms. In order to validate the coupled method proposed in this paper, one of the most common failure modes, i.e., wedge failure, is analyzed by the algorithm and its results are compared with that of physical model tests (Yeung et al. [17]).

As shown in Fig. 5, the model considered in Ref. [17] consisted of a plaster wedge block placed on a plaster supporting block, which contained the "mould" of the wedge block. The supporting block was attached to a wood base block, which in its turn was attached to a tilt table inclined at an angle α with the horizontal direction. The wedge block could move freely without being obstructed by the tilt table. The orientation of the model was quantified by angle β between the tilt table dip direction and the orthogonal to the wedge intersection vector. In each test, the model was fixed in a desired position corresponding to the chosen α and β; the wedge block was held in place and then released. Two different wedge blocks, named Block 1 and Block 2, are considered and their dimensions are shown in Fig. 6. The angle α varied from 0° to 90° in 10° increments while the angle β was equal to 60°, 80° and 240° for Block 1 and equal to 60°, 80° and 320° for Block 2. The coordinates of the block vertices in these cases can be found in Ref. [40]. Figure 6 also shows the possible wedge sliding directions (Direction 1 or Direction 2). Each wedge block was bounded by two joint planes (Plane 1 and Plane 2) and two free surfaces. The average friction angle determined in Ref. [17] from 10 direct shear test measurements was equal to 32.5°; the density of the blocks was 1 400 kg/m^3; the Young's modulus was 10 MPa; the Poisson's ratio was 0.49.

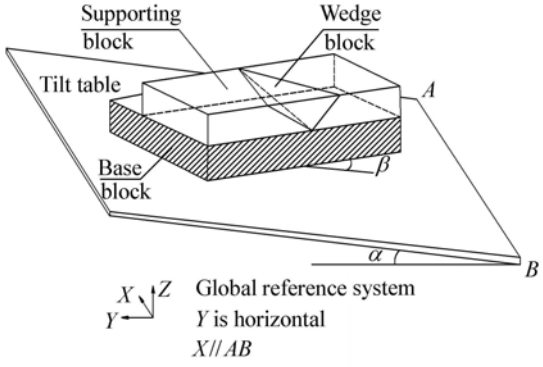

Fig. 5 Physical model of wedge [17]

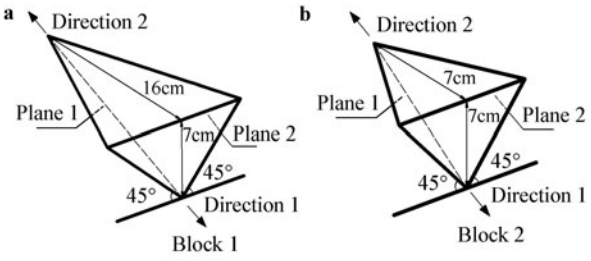

Fig. 6 Wedge blocks [17]

Tables 1 and 2 show detailed results of the presented coupled method and their comparison with physical model results. In order to determine the failure mode and sliding direction, the steepest decent directions of Plane 1 and Plane 2 and Direction 1 or Direction 2 are also listed in Tables 1 and 2. In the coupled method, the sliding direction is determined based on the direction of centroid displacement. For Block 1 shown in Table 1, the failure modes predicted by the coupled method agree very well with model test results without disagreement. The sliding direction of each case is consistent with Direction 1, or Direction 2, or the steepest decent direction of Plane 1 or Plane 2. For Block 2 as shown in Table 2, most of the failure modes predicted by the coupled method agree with the physical model results. Disagreement occurs only for 3 cases out of 32 cases. For these three cases with $\beta = 60°$ and $\alpha = 70°$, 80° or 90°, respectively, the failure modes predicted by the present coupled method are all "free fall", while the results determined by model tests [17] are translational sliding on Plane 2. It can be seen from Table 2 that the direction of centroid displacement, which is the direction of free falling, is very close to the steepest decent direction of Plane 2. The safety factors based on block theory for these three cases are 0, 0.07 and 0.14 [17], respectively. So the differences probably originate from the measurement error in physical model tests and numerical error in the coupled method. For case with $\beta = 320°$ and $\alpha = 85°$, the failure mode predicted by the coupled method is translational and torsional sliding (TTS) on Plane 2 as shown in Fig. 7, which also agrees with the model test results, while the result determined by Block Theory [17] is translational sliding on Plane 2. The TTS failure mode was also predicted by Tonon and Asadollahi [40] using the BS3D algorithm developed by Tonon [41]. So the differences probably originate from the limit of the Block Theory.

5 Application

A realistic rockslide is modeled by the coupled method to illustrate the ability and advantage of DDA coupled with FEM. Figure 8 shows the computational model of Jiweishan rockslide which happened in Chongqing, China in 2009. According to the realistic phenomenon, there are three blocks including B1, B2 and B3 in this model, as shown in Fig. 8. B1 is fixed and also referred to as the stable bedrock. B1, B2 and B3 are discretized into 123, 86 and 9 tetrahedron elements, respectively. Figure 8c shows the size and sliding direction of the rock slope. The parameters of joints (shown in Fig. 8d) and blocks material are listed in Table 3. The time interval is set as 0.01 s and totally 10 000 steps are simulated. The first four thousand steps, which constitute time duration of 40 s, are static analyses used to simulate original gravity force field.

Table 1 Results from the coupled method and physical model tests [17] for Block 1

β	α	Steepest decent direction of Plane 1			Steepest decent direction of Plane 2			Direction 1 or 2			Results from the coupled method				Physical model results
		x	y	z	x	y	z	x	y	z	Direction of centroid displacement			Failure mode	
60	0	−0.40	0.54	−0.74	0.67	−0.07	−0.74	0.46	0.79	−0.40	–	–	–	stable	stable
60	10	−0.30	0.48	−0.83	0.68	0.03	−0.73	0.46	0.71	−0.53	–	–	–	stable	stable
60	18.3	−0.22	0.40	−0.89	0.66	0.12	−0.74	**0.46**	**0.63**	**−0.63**	**0.45**	**0.63**	**−0.63**	w1	w1
60	20	−0.21	0.38	−0.90	0.65	0.14	−0.75	**0.46**	**0.61**	**−0.65**	**0.45**	**0.61**	**−0.65**	w1	w1
60	30	−0.13	0.26	−0.96	0.59	0.21	−0.78	**0.46**	**0.49**	**−0.74**	**0.45**	**0.49**	**−0.75**	w1	w1
60	40	−0.06	0.12	−0.99	0.51	0.26	−0.82	**0.46**	**0.35**	**−0.82**	**0.44**	**0.36**	**−0.82**	w1	w1
60	50	0.01	−0.02	−1.00	**0.42**	**0.27**	**−0.87**	0.46	0.20	−0.87	**0.41**	**0.26**	**−0.87**	p2	p2
60	60	0.08	−0.16	−0.98	**0.33**	**0.24**	**−0.91**	0.46	0.05	−0.89	**0.33**	**0.24**	**−0.92**	p2	p2
60	70	0.15	−0.29	−0.95	**0.24**	**0.20**	**−0.95**	0.46	−0.11	−0.88	**0.23**	**0.20**	**−0.95**	p2	p2
60	80	0.23	−0.41	−0.88	**0.15**	**0.13**	**−0.98**	0.46	−0.26	−0.85	**0.14**	**0.13**	**−0.98**	p2	p2
60	90	0.32	−0.50	−0.80	**0.06**	**0.06**	**−1.00**	0.46	−0.40	−0.79	**0.06**	**0.05**	**−1.00**	p2	p2
80	0	−0.56	0.37	−0.74	0.66	0.16	−0.74	0.16	0.90	−0.40	–	–	–	stable	stable
80	10	−0.45	0.38	−0.80	0.59	0.24	−0.77	0.16	0.82	−0.55	–	–	–	stable	stable
80	17.17	−0.38	0.36	−0.85	0.53	0.27	−0.80	**0.16**	**0.74**	**−0.65**	**0.16**	**0.75**	**−0.65**	w1	w1
80	20	−0.35	0.35	−0.87	0.50	0.28	−0.82	**0.16**	**0.71**	**−0.69**	**0.16**	**0.71**	**−0.68**	w1	w1
80	30	−0.25	0.28	−0.92	0.41	0.28	−0.87	**0.16**	**0.58**	**−0.80**	**0.15**	**0.58**	**−0.80**	w1	w1
80	40	−0.16	0.20	−0.97	0.32	0.25	−0.91	**0.16**	**0.43**	**−0.89**	**0.16**	**0.44**	**−0.89**	w1	w1
80	50	−0.08	0.10	−0.99	0.23	0.20	−0.95	**0.16**	**0.27**	**−0.95**	**0.15**	**0.28**	**−0.95**	w1	w1
80	60	0.01	−0.01	−1.00	**0.14**	**0.13**	**−0.98**	0.16	0.10	−0.98	**0.13**	**0.14**	**−0.98**	p2	p2
80	70	0.09	−0.12	−0.99	**0.05**	**0.05**	**−1.00**	0.16	−0.07	−0.98	**0.05**	**0.05**	**−1.00**	p2	p2
80	80	0.18	−0.22	−0.96	−0.04	−0.04	−1.00	0.16	−0.24	−0.96	0.00	0.00	−1.00	free fall	free fall
80	90	0.27	−0.30	−0.91	−0.13	−0.12	−0.98	0.16	−0.40	−0.90	0.00	0.00	−1.00	free fall	free fall
240	0	0.40	−0.54	−0.74	−0.67	0.07	−0.74	−0.46	−0.79	−0.40	–	–	–	stable	stable
240	10	0.52	−0.56	−0.64	−0.63	0.17	−0.76	−0.46	−0.85	−0.26	–	–	–	stable	stable
240	20	0.67	−0.50	−0.55	−0.56	0.24	−0.79	−0.46	−0.88	−0.11	–	–	–	stable	stable
240	30	0.82	−0.33	−0.47	−0.48	0.26	−0.84	0.46	0.89	−0.05	–	–	–	stable	stable
240	40	0.90	−0.04	−0.44	−0.38	0.26	−0.89	0.46	0.87	−0.20	–	–	–	stable	stable
240	50	0.85	0.26	−0.46	−0.29	0.23	−0.93	0.46	0.82	−0.35	–	–	–	stable	stable
240	60	0.71	0.47	−0.52	−0.20	0.17	−0.96	0.46	0.74	−0.49	–	–	–	stable	stable
240	68.1	0.59	0.55	−0.60	−0.13	0.12	−0.98	**0.46**	**0.67**	**−0.59**	**0.38**	**0.64**	**−0.67**	w2	w2
240	70	0.56	0.55	−0.61	−0.11	0.10	−0.99	**0.46**	**0.65**	**−0.61**	**0.39**	**0.62**	**−0.68**	w2	w2
240	80	**0.43**	**0.55**	**−0.71**	−0.03	0.02	−1.00	0.46	0.53	−0.71	**0.36**	**0.55**	**−0.75**	p1	p1
240	90	**0.32**	**0.50**	**−0.80**	0.06	−0.06	−1.00	0.46	0.40	−0.79	**0.31**	**0.46**	**−0.83**	p1	p1

Note: w1 and w2 mean wedge translational sliding along Direction 1 or Direction 2, respectively, as illustrated in Fig. 6. p1 and p2 mean translational sliding on Plane 1 only or on Plane 2 only respectively, – means stable.

Table 2 Results from the coupled method and physical model tests [17] for Block 2

β	α	Steepest decent direction of Plane 1			Steepest decent direction of Plane 2			Direction 1 or 2			Results from the coupled method				Physical model results
		x	y	z	x	y	z	x	y	z	Direction of centroid displacement			Failure mode	
60	0	0.15	−0.56	−0.82	−0.56	−0.15	−0.82	**−0.35**	**−0.61**	**−0.71**	**−0.35**	**−0.61**	**−0.71**	w1	w1
60	10	0.10	−0.42	−0.90	−0.50	−0.19	−0.85	**−0.35**	**−0.48**	**−0.80**	**−0.35**	**−0.48**	**−0.80**	w1	w1
60	20	0.06	−0.27	−0.96	−0.42	−0.21	−0.88	**−0.35**	**−0.33**	**−0.87**	**−0.35**	**−0.34**	**−0.87**	w1	w1
60	30	0.02	−0.10	−0.99	**−0.34**	**−0.20**	**−0.92**	−0.35	−0.18	−0.92	**−0.33**	**−0.23**	**−0.92**	p2	p2
60	40	−0.01	0.06	−1.00	**−0.25**	**−0.17**	**−0.95**	−0.35	−0.01	−0.94	**−0.24**	**−0.19**	**−0.95**	p2	p2
60	50	−0.05	0.23	−0.97	**−0.17**	**−0.12**	**−0.98**	−0.35	0.15	−0.92	**−0.17**	**−0.13**	**−0.98**	p2	p2
60	60	−0.09	0.38	−0.92	**−0.08**	**−0.06**	**−0.99**	−0.35	0.31	−0.88	**−0.08**	**−0.07**	**−0.99**	p2	p2
60	70	−0.14	0.53	−0.84	0.00	0.00	−1.00	−0.35	0.46	−0.82	0.00	0.00	**−1.00**	free fall	p2
60	80	−0.19	0.65	−0.74	0.09	0.07	−0.99	−0.35	0.59	−0.73	0.00	0.00	**−1.00**	free fall	p2
60	90	−0.27	0.74	−0.61	0.17	0.12	−0.98	−0.35	0.71	−0.61	0.00	0.00	**−1.00**	free fall	p2
80	0	0.33	−0.47	−0.82	−0.47	−0.33	−0.82	**−0.12**	**−0.70**	**−0.71**	**−0.12**	**−0.69**	**−0.72**	w1	w1
80	10	0.24	−0.39	−0.89	−0.37	−0.31	−0.87	**−0.12**	**−0.56**	**−0.82**	**−0.12**	**−0.56**	**−0.82**	w1	w1
80	20	0.15	−0.27	−0.95	−0.28	−0.26	−0.92	**−0.12**	**−0.41**	**−0.90**	**−0.12**	**−0.41**	**−0.90**	w1	w1
80	30	0.08	−0.15	−0.99	−0.18	−0.19	−0.96	**−0.12**	**−0.25**	**−0.96**	**−0.12**	**−0.25**	**−0.96**	w1	w1
80	40	0.01	−0.01	−1.00	−0.10	−0.10	−0.99	−0.12	−0.08	−0.99	**−0.09**	**−0.12**	**−0.99**	p2	p2
80	50	−0.07	0.12	−0.99	−0.01	−0.01	−1.00	−0.12	0.09	−0.99	**−0.01**	**−0.02**	**−1.00**	p2	p2
80	60	−0.14	0.25	−0.96	0.08	0.09	−0.99	−0.12	0.26	−0.96	0.00	0.00	**−1.00**	free fall	free fall
80	70	−0.22	0.37	−0.90	0.17	0.18	−0.97	−0.12	0.43	−0.90	0.00	0.00	**−1.00**	free fall	free fall
80	80	−0.32	0.46	−0.83	0.26	0.25	−0.93	−0.12	0.58	−0.81	0.00	0.00	**−1.00**	free fall	free fall
80	90	−0.42	0.52	−0.74	0.35	0.31	−0.88	−0.12	0.71	−0.70	0.00	0.00	**−1.00**	free fall	free fall
320	0	−0.58	-0.05	−0.82	−0.05	0.58	−0.82	**−0.54**	**0.45**	**−0.71**	**−0.54**	**0.45**	**−0.71**	w1	w1
320	10	−0.54	-0.11	−0.83	−0.07	0.71	−0.70	**−0.54**	**0.57**	**−0.62**	**−0.54**	**0.56**	**−0.63**	w1	w1
320	10.3	−0.54	-0.12	−0.83	−0.07	0.71	−0.70	**−0.54**	**0.57**	**−0.61**	**−0.54**	**0.56**	**−0.63**	w1	w1
320	20	−0.49	−0.16	−0.86	−0.10	0.81	−0.57	**−0.54**	**0.67**	**−0.51**	**−0.55**	**0.64**	**−0.54**	w1	w1
320	30	−0.43	−0.18	−0.89	−0.15	0.89	−0.42	−0.54	0.75	−0.39	–	–	–	stable	stable
320	40	−0.35	−0.18	−0.92	−0.26	0.93	−0.26	−0.54	0.80	−0.25	–	–	–	stable	stable
320	50	−0.27	−0.16	−0.95	−0.66	0.75	−0.11	−0.54	0.83	−0.11	–	–	–	stable	stable
320	60	−0.19	−0.12	−0.97	−0.60	−0.79	−0.12	0.54	−0.84	−0.04	–	–	–	stable	stable
320	70	−0.11	−0.07	−0.99	−0.25	−0.93	−0.27	0.54	−0.82	−0.19	–	–	–	stable	stable
320	80	−0.02	−0.02	−1.00	−0.15	−0.89	−0.43	0.54	−0.78	−0.32	–	–	–	stable	stable
320	85	0.02	0.01	−1.00	−0.12	−0.85	−0.51	0.54	−0.74	−0.39	−0.12	−0.82	−0.56	TTS	TTS
320	90	0.06	0.04	−1.00	**−0.10**	**−0.81**	**−0.58**	0.54	−0.71	−0.45	**0.08**	**−0.81**	**−0.59**	p2	p2

Note: w1 and w2 mean respectively wedge translational sliding along Direction 1 or Direction 2 as illustrated in Fig. 6. p1 and p2 mean translational sliding on Plane 1 only or on Plane 2 only, respectively. TTS means translational and torsional sliding on Plane 2, – means stable.

Table 3 Parameters of joints and blocks [42]

Matarial	c/kPa	ϕ/(°)	E/GPa	μ	ρ/(kg·m^{-3})
J1	0	8	–	–	–
J2	200	20	–	–	–
J3	200	8	–	–	–
J4	50	20	–	–	–
J5	300	25	–	–	–
B1	–	–	25	0.24	2 600
B2	–	–	25	0.24	2 600
B3	–	–	25	0.24	2 000

Note: J5 is the interface of B2 and B3.

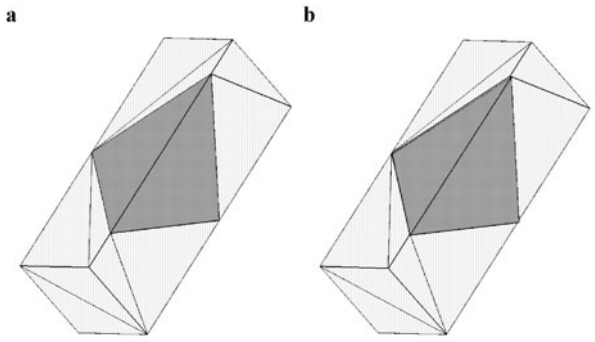

Fig. 7 Failure mode for Block 2 with initial configuration of $\beta = 320°$ and $\alpha = 85°$. **a** Initial configuration; **b** Failure mode

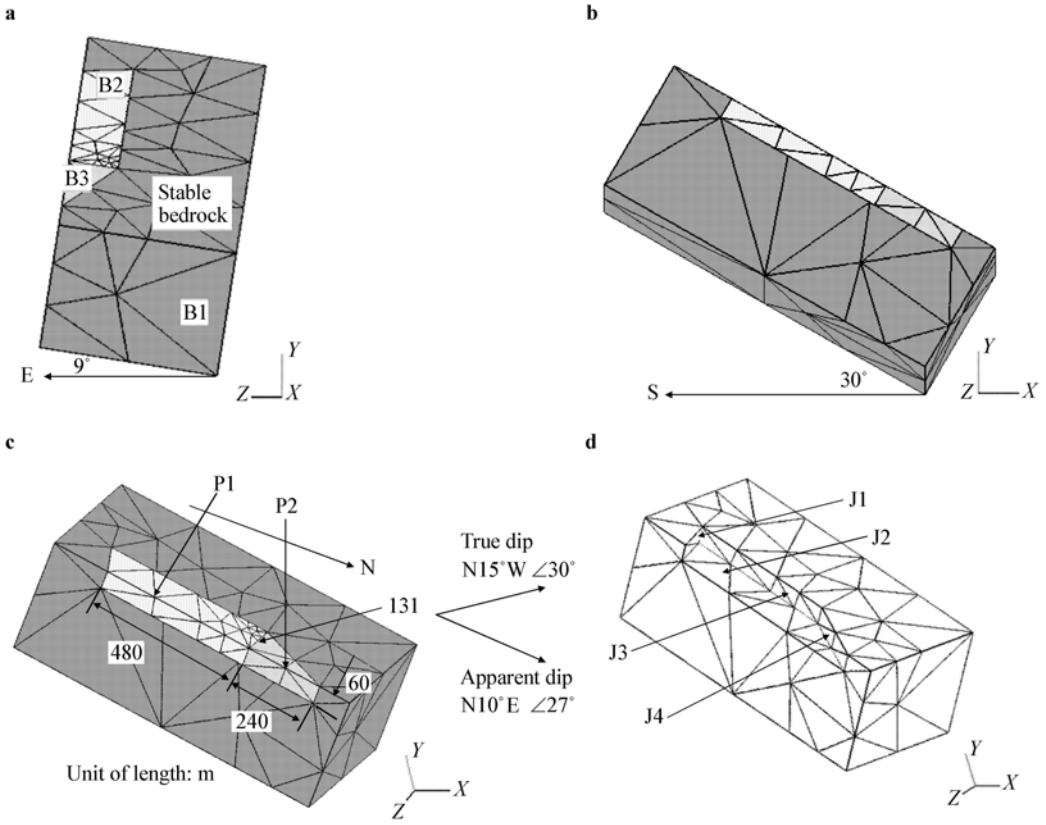

Fig. 8 Computational model of Jiweishan rockslide. **a** Left view; **b** Front view; **c** Iso view; **d** Joints

Figure 9 shows the sliding process of rock blocks at several specific moments. Figures 10 and 11 show the displacement and velocity history of two specific points of P1 and P2, which are respectively on B2 and B3 as shown in Fig. 8c. From Fig. 10 it can be seen that the displacements of P1 and P2 increase very slowly with time steps in the first 40 static analysis, which means that B2 and B3 are unstable under gravity load. Because the gravity of B2 is the primary driving force, B2 is named as driving block. In the coupled method, the velocity of the nodal points is set as zero in the first 40 s to simulate static process as shown in Fig. 11. The slope profile at the end of 40 s static analysis is shown in Fig. 9a. Thereafter dynamic analysis is used to simulate the sliding process of the rock slope under gravity. At 45 s the driving block B2 is separated obviously from the stable bedrock B1, as shown in Fig. 9b. At 49 s in Fig. 9c, the joint J5 between B2 and B3 is detached and B3 is moving to the margin of the cliff of the bedrock. At 55 s B3 is toppling down from the bedrock and going on a free falling down movement as shown in Fig. 9d. This can also be seen

in Figs. 10b and 11b with the displacement and velocity of P2 increasing sharply along the *y*-direction. At 59 s the driving block B2 is also moving close to the edge of the bedrock and at 63 s it is toppling down from the slope as shown in Figs. 9e and 9f, respectively.

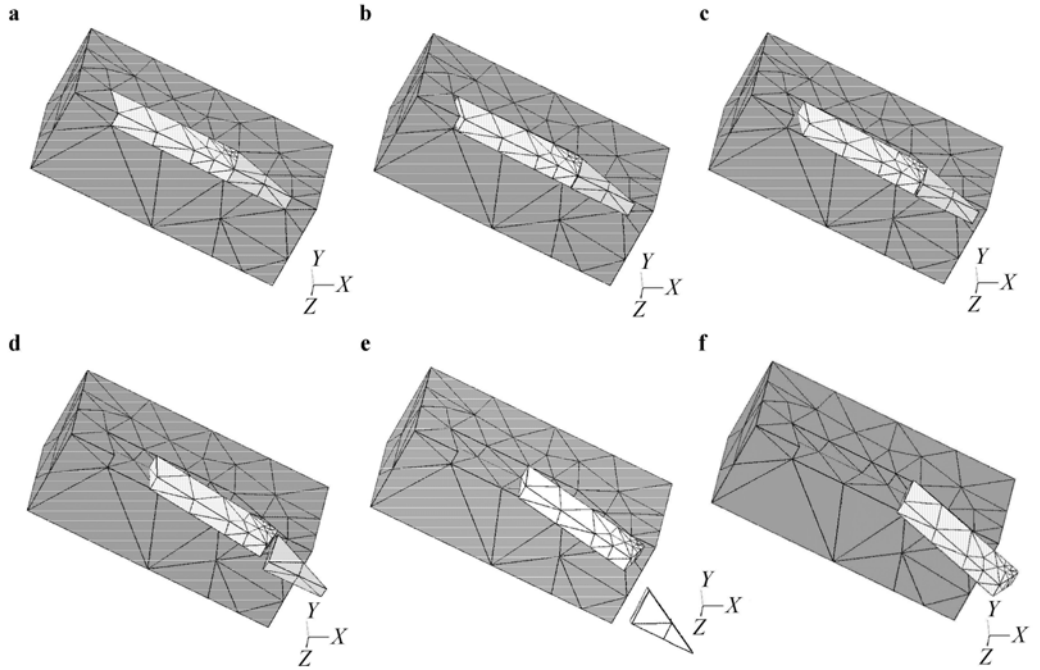

Fig. 9 The sliding process of rock blocks. **a** 40 s; **b** 45 s; **c** 49 s; **d** 55 s; **e** 59 s; **f** 63 s

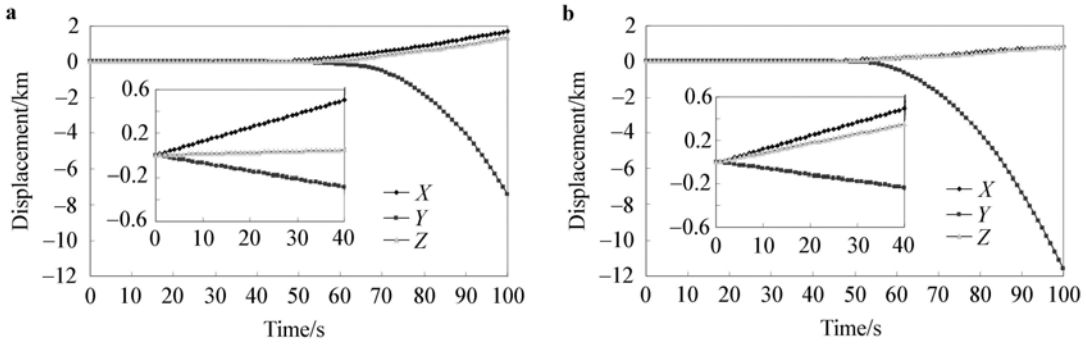

Fig. 10 The displacement history of two specific points. **a** P1 on B2; **b** P2 on B3

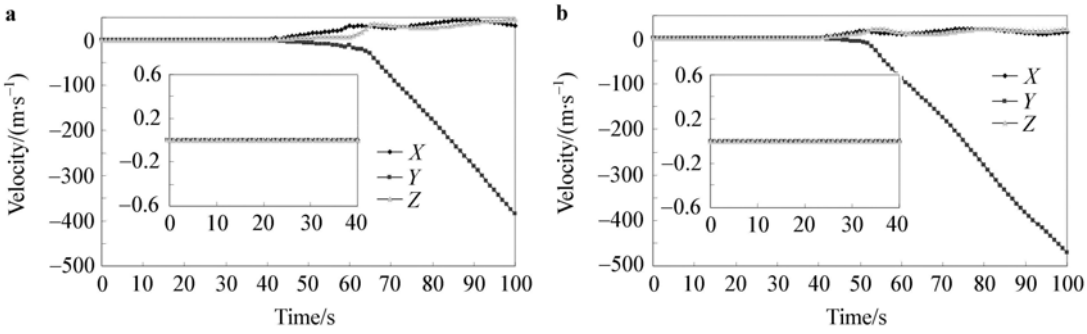

Fig. 11 The velocity history of two specific points. **a** P1 on B2; **b** P2 on B3

6 Conclusions

In this paper, 3D DDA is coupled with tetrahedron finite elements to tackle the problem of block expansion and to enhance DDA block's deformation ability. Tetrahedron is the simplest in the 3D domain, and it is easy to implement automatic discretization even for complex topology shape. Furthermore, block faces may not remain planar for hexahedron finite elements or high order displacement functions after deformation, which will cause contact detection difficulties using existing 3D contact detection schemes. However, element faces will remain planar and element edges will remain straight after deformation for tetrahedron finite elements, and thus 3D polyhedral contact detection schemes can be used directly. Therefore, tetrahedron finite elements are appropriate for being meshed into 3D DDA blocks. The matrices of equilibrium equations for this coupled method are given in detail in this paper and a modified fast common plane method is suggested for contact detection. For validation, one of the most common failure modes, i.e., wedge failure, is analyzed by the coupled method and its results are compared with that of physical model tests (Yeung et al. [17]). Most of the failure modes predicted by the coupled method agree with the physical model results except for 3 cases out of the total 65 cases. Finally, a complex rockslide example demonstrates the robustness and versatility of the coupled method.

References

1 Shi, G.H., Goodman, R.E.: Two dimensional discontinuous deformation analysis. International Journal for Numerical and Analytical Methods in Geomechanics **9**, 541–556 (1985)

2 Shi, G.H.: Discontinuous deformation analysis a new numerical model for the statics and dynamics of block systems. [Ph.D. Thesis]. Department of Civil Engineering, UC Berkeley, California, USA (1989)

3 MacLaughlin, M.M., Doolin, D.M.: Review of validation of the discontinuous deformation analysis (DDA) method. International Journal for Numerical and Analytical Methods in Geomechanics **30**, 271–305 (2006)

4 Koo, C.F., Chern, J.C., Chen, S.: Development of second-order displacement function for DDA. In: Proceedings of ICADD-1, the First International Conference on Analysis of Discontinuous Deformation, Taiwan, China 1–23 (1995)

5 Ma, M.Y., Zaman, M., Zhou, J.H.: Discontinuous deformation analysis using the third-order displacement function. In: Proceedings of the First International Forum on Discontinuous Deformation Analysis (Dda) and Simulations of Discontinuous Media. USA, TSI Press, 383–394 (1996)

6 Lin, J.S., Lee, D.H.: Manifold method using polynomial basis function of any order. In: Proceedings of the First International Forum on Discontinuous Deformation Analysis (DDA) and Simulations of Discontinuous Media, USA, TSI Press, 365–372 (1996)

7 Ke, T.C.: Artificial joint-based DDA. In: Proceedings of the First International Forum on Discontinuous Deformation Analysis (DDA) and Simulations of Discontinuous Media, USA, TSI Press, 326–333 (1996)

8 Cheng, Y.M., Zhang, Y.H.: Rigid body rotation and block internal discretization in DDA analysis. International Journal for Numerical and Analytical Methods in Geomechanics **24**, 567–578 (2000)

9 Ning, Y.J., Yang, J., An, X.M., et al.: Modelling rock fracturing and blast-induced rock mass failure via advanced discretisation within the discontinuous deformation analysis framework. Computers and Geotechnics **38**, 40–49 (2011)

10 Shyu, K.: Nodal-based discontinuous deformation analysis. [Ph.D. Thesis]. University of California, Berkeley, USA (1993)

11 Chang, C.T.: Nonlinear dynamic discontinuous deformation analysis with finite element meshed block systems. [Ph.D. Thesis]. University of California, Berkeley, USA (1994)

12 Jing, L., Ma, Y., Fang, Z.: Modeling of fluid flow and solid deformation for fractured rocks with discontinuous deformation analysis (DDA) method. International Journal of Rock Mechanics and Mining Science **38**, 343–355 (2001)

13 Grayeli, R., Mortazavi, A.: Discontinuous deformation analysis with second-order finite element meshed block. International Journal for Numerical and Analytical Methods in Geomechanics **30**, 1545–1561 (2006)

14 Ke, T.C.: The issue of rigid body rotation in DDA. In: Proceedings of the First International Forum on Discontinuous Deformation Analysis (DDA) and Simulations of Discontinuous Media. USA, TSI Press, 318–325 (1996)

15 Shi, G.H.: Three dimensional discontinuous deformational analyses. In: Bicanic, N., ed. Proceedings of the Fourth International Conference on Analysis of Discontinuous Deformation (ICADD-4). University of Glasgow Scotland, UK, 1–21 (2001)

16 Liu, J., Kong, X.J., Lin, G.: Formulations of the three-dimensional discontinuous deformation analysis method. Acta Mechanica Sinica **20**, 270–282 (2004)

17 Yeung, M.R., Jiang, Q.H., Sun, N.: Validation of block theory and three-dimensional discontinuous deformation analysis as wedge stability analysis methods. International Journal of Rock Mechanics and Mining Science **40**, 265–275 (2003)

18 Moosavi, M., Jafari, A., Beyabanaki, S.A.R.: Dynamic three-dimensional discontinuous deformation analysis (3-D DDA) validation using analytical solution. In: Proceedings of the Seventh International Conference on Analysis of Discontinuous Deformation (ICADD-7), Hawaii, USA, 37–48 (2005)

19 Cundall, P.A.: Formulation of a three-dimensional distinct element model—Part I: A scheme to detect and represent contacts in a system composed of many polyhedral blocks. International Journal of Rock Mechanics and Mining Sciences **25**, 107–116 (1988)

20 Nezami, E.G., Hashash, Y.M.A., Zhao, D.W., et al.: A fast contact detection algorithm for 3-D discrete element method. Computers and Geotechnics **31**, 575–587 (2004)

21 Beyabanaki, S.A.R., Mikola, R.G., Hatami, K.: Three-dimensional discontinuous deformation analysis (3-D DDA) using a new contact resolution algorithm. Computers and Geotechnics **35**, 346–356 (2008)

22 Keneti, A.R., Jafari, A., Wu, J.H.: A new algorithm to identify contact patterns between convex blocks for three-dimensional discontinuous deformation analysis. Computers and Geotechnics **35**, 746–759 (2008)

23 Jiang, Q.H., Yeung, M.R.: A model of point-to-face contact for

three-dimensional discontinuous deformation analysis. Rock Mechanics and Rock Engineering **37**, 95–116 (2004)

24 Yeung, M.R., Jiang, Q.H., Sun, N.: A model of edge-to-edge contact for three-dimensional discontinuous deformation analysis. Computers and Geotechnics **34**, 175–186 (2007)

25 Beyabanaki, S.A.R., Jafari, A., Yeung, M.R.: High-order three-dimensional discontinuous deformation analysis (3-D DDA). International Journal for Numerical Methods in Biomedical Engineering **26**, 1522–1547 (2010)

26 Liu, J., Kong, X.J.: Three dimensional continuous and discontinuous deformation analysis. Acta Mechanica Sinica **34**, 941–948 (2002) (in Chinese)

27 Beyabanaki, S.A.R., Jafari, A., Biabanaki, S.O.R., et al.: Nodal-based three-dimensional discontinuous deformation ana-lysis (3-D DDA). Computers and Geotechnics **36**, 359–372 (2009)

28 Wu, J.H., Ohnishi, Y., Nishiyama, S.: A development of the discontinuous deformation analysis for rock fall analysis. International Journal for Numerical and Analytical Methods in Geomechanics **29**, 971–988 (2005)

29 Zienkiewicz, O.C., Taylor, R.L.: Finite Element Method. Butterworth Heinemann, London (2000)

30 Benzley, S.E., Perry, E., Merkley, K., et al.: A comparison of all-hexahedral and all-tetrahedral finite element meshes for elastic and elasto-plastic analysis. In: Proceedings of 4th International Meshing Roundtable, Sandia National Laboratories, USA, 179–191 (1995)

31 Grayeli, R., Hatami, K.: Implementation of the finite element method in the three-dimensional discontinuous deformation analysis (3D-DDA). Int. J. Numer. Anal. Meth. Geomech. **32**, 1883–1902 (2008)

32 Zheng, H., Jiang, W.: Discontinuous deformation analysis based on complementary theory. Science in China Series E: Technological Sciences **52**, 2547–2554 (2009)

33 Wei, J., Hong, Z.: Discontinuous deformation analysis based on variational inequality theory. International Journal of Computational Methods **8**, 193–208 (2011)

34 Shi, G.H.: New Numerical Method of Block System's Discontinuous Deformation Analysis. Ren, F., transl. Science Press, Beijing (1993)

35 Barbosa, R.E.: Discrete element models for granular materials and rock masses. [Ph.D. Thesis]. Department of Civil and Environmental Engineering, University of Illinois at Urbana-Champaign. Urbana, USA (1990)

36 Williams, J.R., O'Connor, R.: A linear complexity intersection algorithm for discrete element simulations of arbitrary geometries. International Journal for CAE-Engineering Computation, Special Ed Discrete Element Method **12**, 185–201 (1995)

37 Krishnasamy, J., Jakiela, M.J.: A method to resolve ambiguities in corner–corner interactions polygons in the context of motion simulation. Engineering Computation **12**, 135–144 (1995)

38 Feng, Y.T., Owen, D.R.J.: An energy based corner to contact algorithm. In: Cook, B.K., Jensen, R.P., eds. Discrete Element Methods, Numerical Modeling of Discontinua. Santa Fe, New Mexico, USA, 32–37 (2002)

39 Geng, Q.D.: Improvement on common plane detection algorithm and three-dimensional discrete particles generation algorithm. [Master Thesis]. Dalian, Dalian University of Technology, China (2009)

40 Tonon, F., Asadollahi, P.: Validation of general single rock block stability analysis (BS3D) for wedge failure. International Journal of Rock Mechanics & Mining Sciences **45**, 627–637 (2008)

41 Tonon, F.: Analysis of single rock blocks for general failure modes under conservative and non-conservative forces. International Journal for Numerical and Analysis Methods in Geomechanics **31**, 1567–1608 (2007)

42 Yin, Y.P., Sun, P., Zhang, M., et al.: Mechanism on apparent dip sliding of oblique inclined bedding rockslide at Jiweishan, Chongqing, China. Landslides **8**, 49–65 (2011)